scientific reports

Check for updates

OPEN

A cutting-edge neural network approach for predicting the thermoelectric efficiency of defective gamma-graphyne nanoribbons

Jiayi Guo[1,2,3], Chunfeng Cui[1,3], Tao Ouyang[1], Juexian Cao[1]✉ & Xiaolin Wei[1,2]✉

This study predicts the thermoelectric figure of merit (ZT) for defective gamma-graphyne nanoribbons (γ-GYNRs) using binary coding, convolutional neural networks (CNN), long short-term memory networks (LSTM), and multi-scale feature fusion. The approach accurately predicts ZT values with only 500 initial structures (3% of 16,512 candidates), achieving an R^2 above 0.91 and a mean absolute error (MAE) of 0.05 to 0.06. The use of artificial feature extraction combined with an attention mechanism reveals that the number and distribution of defects are crucial for achieving high ZT values. γ-GYNRs with moderate and evenly distributed defect count show superior thermoelectric performance. This demonstrates the effectiveness of neural networks in designing low-dimensional materials like γ-GYNRs and offers insights into exploring other materials with excellent thermoelectric properties.

Keywords Thermoelectric figure of merit, Graphyne nanoribbons, Convolutional neural networks, Long short-term memory networks, Multi-scale feature fusion, Attention mechanism

Owing to the distinctive capacity of direct conversion between electrical and thermal energy, thermoelectric materials have become a promising avenue for improving energy efficiency and advancing sustainable energy technologies. Such materials are able to utilize waste heat, solar energy or ambient temperature differences for effective energy recovery and conversion, and also play an important role in refrigeration[1–3]. The key performance indicator of thermoelectric materials is thermoelectric figure of merit (ZT), which is a key parameter to measure the thermoelectric conversion efficiency of materials. High-performance thermoelectric materials tend to possess high Seebeck coefficient, high electrical conductivity, and low thermal conductivity[4]. Common thermoelectric materials can be classified into traditional bulk thermoelectric materials[5,6], polymer thermoelectric materials[7,8], and emerging low-dimensional materials[9–11]. Among the numerous low-dimensional thermoelectric materials, 2D materials are emerged as a subject of intense research interest in the field of thermoelectricity due to their tunable electronic properties, low thermal conductivity, and high thermoelectric power[12,13].

As a representative of 2D materials, graphene exhibits remarkable properties, including unique electronic, mechanical, and topological properties, which belong to the hot spot in present physical and material research community[14,15]. Graphyne, an extended form of graphene, also exhibits fascinating physical and chemical properties, and endows the competitive in 2D materials[16–18]. Theoretical calculations indicate that graphyne and its derivatives exhibit a distinctive Dirac cone structure[19,20], high carrier mobility[21,22], unique mechanical properties[23,24], and excellent thermal stability[25], making them valuable materials for use in electronic devices, energy storage, and other fields[26–32]. Recent significant progress in the experimental synthesis of graphyne[33–36] further promote researchers on such novel 2D materials. Especially, owing to the low thermal conductivity, graphyne is predicted to possess better thermoelectric performance compared to graphene. The first-principles calculations and non-equilibrium Green's function (NEGF) calculations indicate that the thermoelectric figure of merit of γ-GYNRs at room temperature is close to 0.45[37,38], which is approximately one order of magnitude higher than that of graphene. Nevertheless, the thermoelectric performance of γ-GYNRs is still a bit far from

[1]Department of Physics & Hunan Institute of Advanced Sensing and Information Technology, Xiangtan University, Xiangtan 411105, People's Republic of China. [2]College of Physics and Electronics Engineering, Hengyang Normal University, Hengyang 421002, People's Republic of China. [3]Jiayi Guo and Chunfeng Cui contributed equally to this article. ✉email: jxcao@xtu.edu.cn; xlw@xtu.edu.cn

the actual application goal, accordingly exploring some feasible and effective way to enhance the figure of merit is of crucial importance.

Previous studies have proposed a variety of techniques to improve the thermoelectric conversion efficiency, including artificial structure design[39,40], strain control[41], and defect engineering[42,43]. Among these approaches, defect engineering is a common and straightforward method in experiments[44,45], while it is challenging to implement due to the extensive degrees of freedom in structure design. This results in a vast number of potential structures, which can be costly to investigate through simulation or experimentation. To overcome this obstacle, researchers gradually shifted their focus on the thermoelectric work combined with machine learning algorithms[46–48]. Yamawaki et al.[46] solved the trade-off between high conductivity, high Seebeck coefficient and low thermal conductivity by combining the multi-functional transmission calculations of phonons and electrons with Bayesian optimization, and significantly improved the thermoelectric conversion efficiency of graphene nanoribbons (GNRs). Choudhary et al.[47] systematically screened two-dimensional materials for efficient thermoelectric properties using density functional theory and semiclassical transport techniques. They applied a machine learning model to accelerate the pre-screening process, significantly boosting efficiency. Similarly, Han et al.[48] demonstrated a framework for automatic discovery of functional materials using artificial intelligence technology, successfully developed a variety of high-performance thermoelectric materials, and verified these prediction results by density functional theory. The emergence of machine learning-based thermoelectric material exploration provides a new way to efficiently screen and design thermoelectric materials. The neural network algorithm is a computational model that simulates a biological neural network, which handles complex data through progressive nonlinear transformation, and has advantages in the field of thermoelectric materials research[49–51]. Considering the potential of graphyne in thermoelectric, we sought to integrate the neural network algorithm into the construction of γ-GYNRs with edge defects, with the objective of further enhancing their thermoelectric conversion efficiency.

Motivated from the above statements, employing the experimentally synthesized γ-GYNRs as the research object, in this paper we utilize binary coding and neural network algorithms to predict the ZT of defective γ-GYNRs in a comprehensive manner. The results demonstrate that the ZT values of γ-GYNRs for all defects can be accurately predicted using only 500 sets of initial structures. The R^2 exceeded 0.91, and the MAE for the test set was between 0.05 and 0.06. The following section briefly overviews the model structure of edge disorder γ-GYNRs, the theoretical formula of NEGF, and basic framework of the Convolutional Neural Network-Long Short-Term Memory Network (CNN-LSTM) algorithm. We discuss the importance of multi-scale fusion methods and artificial feature extraction combined with attention mechanisms in improving the performance of the CNN-LSTM model for predicting ZT values in the third part. The results indicate that γ-GYNRs with a moderate number of defects and a uniform distribution of defects can exhibit higher ZT values. Finally, by replacing these features with a neural network, classifying and regressing the data with high ZT values, 30 defective γ-GYNRs with the highest ZT values were ultimately obtained.

Model and methods

In Fig. 1, we illustrate the atomic structure of a γ-GYNR with symmetric edge disorder defects. This structure is divided into three parts: two semi-infinite length pristine γ-GYNRs acted as leads, and the central region containing defects. To reduce the interaction between the leads and the defect region, we placed a buffer layer on either side of the central region. Considering the three bond types present in γ-GYNRs, with the acetylene bonds at the edges are the most fragile[52]. In our simulations, we systematically introduced longitudinal line defects by selectively removing carbon atoms to create vacancy-type defects, disrupting the π-conjugation within the nanoribbon. This type of defect was specifically chosen to investigate how periodic structural disruptions, such as the absence of acetylene bonds, impact electronic and thermal transport properties. The acetylene bonds along the longitudinal direction were targeted due to their relatively weak bond strength with benzene rings, making them prone to breakage, a factor relevant for material synthesis and performance optimization. Additionally, we trained and predicted the performance of all edge defect structures generated by acetylene bond dissociation using a binary coding scheme, where "1" and "0" indicate defective and intact units, respectively. For the example system shown in Fig. 1, the descriptor set is {001111000011000}.

In this work, the nonequilibrium Green's function (NEGF) method[53] is used to compute the ZT:

$$ZT = \frac{\sigma S^2}{\kappa_e + \kappa_p} T \tag{1}$$

where σ represents the electrical conductivity, S denotes the Seebeck coefficient, κ_e signifies the electronic thermal conductivity which pertains to the capacity of electrons to conduct heat, κ_p denotes the thermal conductivity contributed by phonons which is indicative of the ability of phonons to conduct heat, and T is the absolute temperature. Here, $\sigma = e^2 L_0$, $S = (eT)^{-1} L_1/L_0$, and $\kappa_e = T^{-1}(L_2 - L_1^2)$, $\kappa_p = T^{-1}(L_2 - L_1^2/L_0)$. Under the framework of NEGF method, these electronic transport properties can be obtained by solving the Lorentzian function[54]:

$$L_n(u,T) = \frac{2}{h}\int_{-\infty}^{+\infty} (E-u)^n \left[-\frac{\partial f_e(E,u,T)}{\partial E}\right] T_e(E)\, dE \tag{2}$$

Equation (2) describes the n^{th} order Lorentz function obtained by integrating the energy E, chemical formula u, electron distribution function f_e, and electronic transmission $T_e(E)$. The detailed calculation methods and procedures are provided in Section S1 of the Supplementary Information.

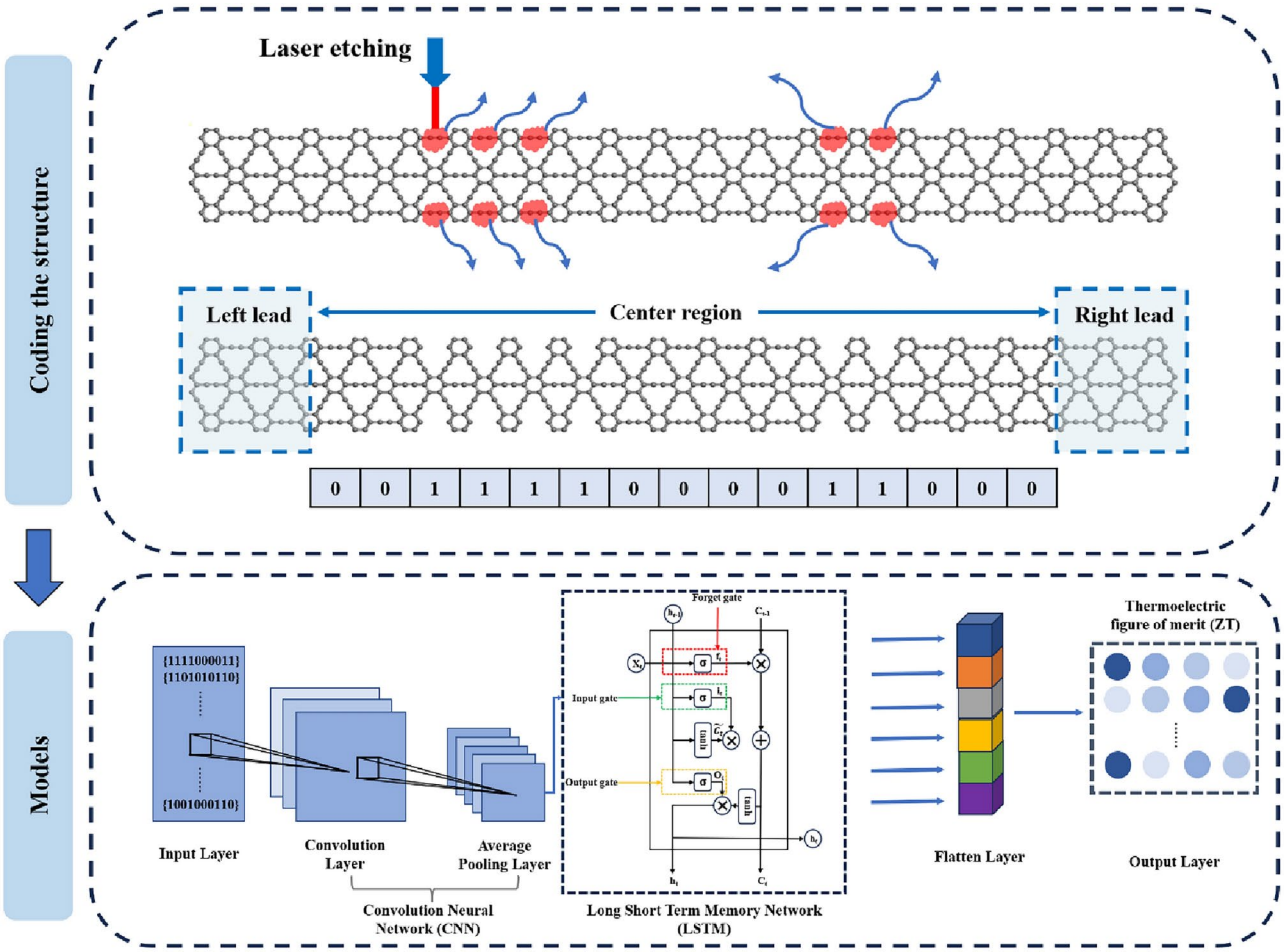

Fig. 1. Methodology for predicting the thermoelectric optima of defective γ-GYNRs structures using CNN-LSTM model. The upper half describes a schematic diagram of the atomic structure of a symmetric defective γ-GYNR and its binary encoding. The lower half describes the construction of the CNN-LSTM model.

In construction of the training model, the input is a 15-dimensional binary code and the ZT value of corresponding edge defective γ-GYNR as the prediction target. Owing to this model host a certain continuity, thus we used the model of CNN-LSTM for training in this work. This is a hybrid neural network that performs feature extraction by convolutional neural network and then sequence prediction by long short-term memory network pairs. In this study, the defective γ-GYNR structure is defined as a defective set, represented by the binary code {001111000011000} in the schematic diagram. Furthermore, assuming that group i is randomly selected from all the alternatives to be used for training, a matrix in the form of an i×j matrix is obtained, where j represents the coding dimension, i.e. the number of defective units. Thus, for such a matrix, feature extraction can be performed by convolutional neural networks. To successfully implement the feature extraction process, a one-dimensional convolutional layer with a number of channels (also known as the number of kernels or filters) of 64 is used to perform the process in conjunction with a Relu function for activation, and then pooling is implemented using an average pooling layer. To prevent overfitting during convolution, a dropout with a probability of 0.2 is added for regularization. This approach effectively prevents the co-action and interconnection of feature detectors to improve the overall performance of the neural network. This segment of the output sequence is used as input to the subsequent long and short-term memory network. To simplify the model, an LSTM network model with a single hidden layer of 50 units is set up for training and prediction. The sequence data is then flattened by the Flatten layer and passed to the fully connected layer (Dense) for regression analysis and prediction.

Results and discussion

In this study, we examined the impact of varying training set sizes on the predictive performance of neural networks by analyzing the model's performance with training set sizes of 400, 500, and 600 groups. Figure 2 illustrates the influence of training set size on R^2 and MAE, showing that as the training set size increases, the R^2 value rises significantly while the MAE declines. This indicates enhanced fitting capacity and prediction accuracy with larger training sets. However, beyond 500 groups, the improvement plateaus, and the marginal benefit diminishes. The inset figure shows a high goodness of fit for all training sizes. For 400 datasets, the

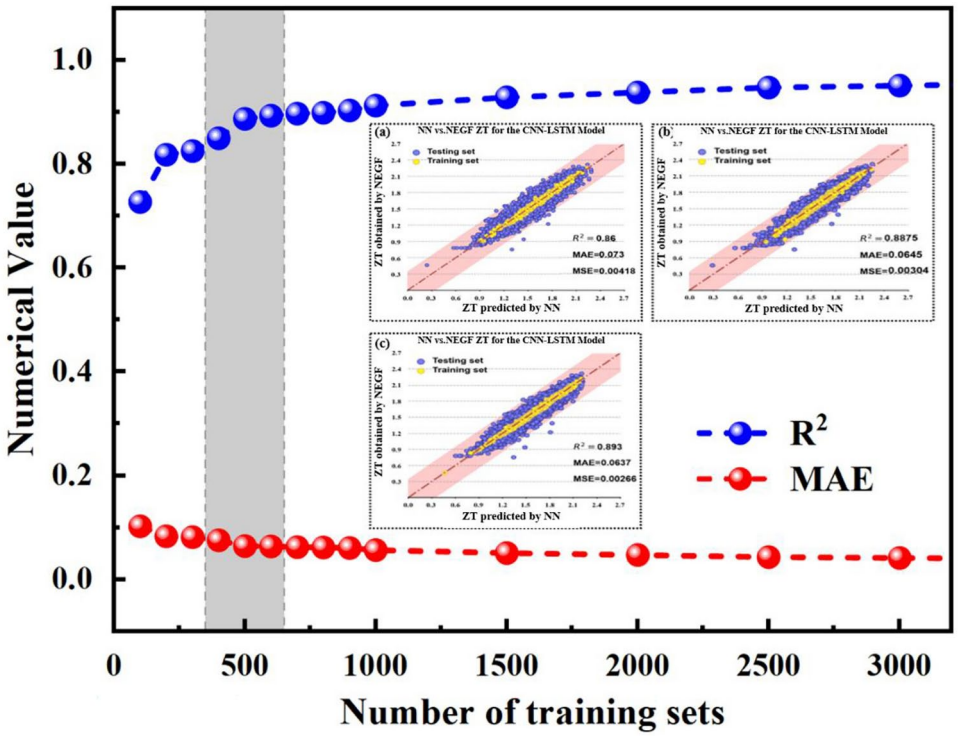

Fig. 2. The effect of size of neural network training set on R^2 and MAE. The insets show the prediction results obtained by training with 400, 500 and 600 sets respectively, with the training set in yellow, representing 3% of the data, and the test set in blue, representing 97% of the data.

model performs well, but with slightly lower R^2 and higher MAE (0.86 and 0.073, respectively). At 500 datasets, both metrics improve significantly, whereas increasing to 600 datasets yields marginal improvements but adds computational complexity. Therefore, 500 datasets balance performance and computational cost, ensuring higher accuracy without excessive computational burden. Consequently, we use 500 datasets for subsequent training and optimization to maintain good generalization and computational efficiency.

Traditional neural network architectures may fall short in capturing intricate features and long-term dependencies, especially with complex time series data, highlighting the need for enhanced prediction performance. To address this, we introduced a more intricate model structure that employs attention mechanisms and multi-scale fusion techniques. Figure 3 illustrates an advanced hybrid architecture of CNN-LSTM with an attention mechanism and multi-scale fusion for feature extraction and prediction of complex time series data. While traditional CNN-LSTM models use convolutional layers for feature extraction and LSTM layers for capturing temporal dependencies, they struggle with single-scale convolutional kernels and lack an attention mechanism. These limitations hinder their ability to capture multi-scale features and focus on key information, thus degrading prediction performance. Our improvements include applying multi-scale convolutional layers to the input data using 3×1, 7×1, and 15×1 kernels, followed by 3×1 average pooling to reduce feature map size and retain key features. This multi-scale convolution captures diverse features, enhancing feature extraction. The pooled feature maps are merged to form a comprehensive representation, integrating multi-scale features. The combined feature maps are then processed through the attention mechanism, which computes query-key similarity to generate attention weights, creating a weighted feature representation. This mechanism helps the model focus on relevant information, improving feature representation and predictive performance. The weighted features are then fed into LSTM layers to capture temporal dependencies, effectively modeling long-term trends. Finally, the LSTM output is used for the model's predictions.

In Fig. 4, we compare the performance of two model architectures on complex time series data. The improved model shows significant enhancement in all indices, demonstrating the effectiveness of multi-scale fusion and attention mechanisms. Figure 4a (left) illustrates the performance of the traditional single-scale CNN-LSTM model. Despite a gradual loss reduction, the convergence is slow, and the final loss value remains high. With 500 data points in the training set, the single-scale model achieves an R^2 of 0.888 on the test set, indicating MAE of 0.065, which is reflecting relatively large prediction errors. This model struggles to capture multi-scale features in the input data, limiting its predictive performance. Figure 4a (right) shows the performance after introducing multi-scale fusion. The improved model exhibits a faster loss reduction rate and a lower final loss value, indicating better convergence. With the same training set, the test set R^2 improves to 0.9, and the MAE drops to 0.06, significantly enhancing prediction accuracy. The multi-scale convolution effectively captures features at different scales, improving model performance. Figure 4b compares different feature selections in the extraction process. The binary coding-only model fails to capture critical features, while introducing artificial features enables the

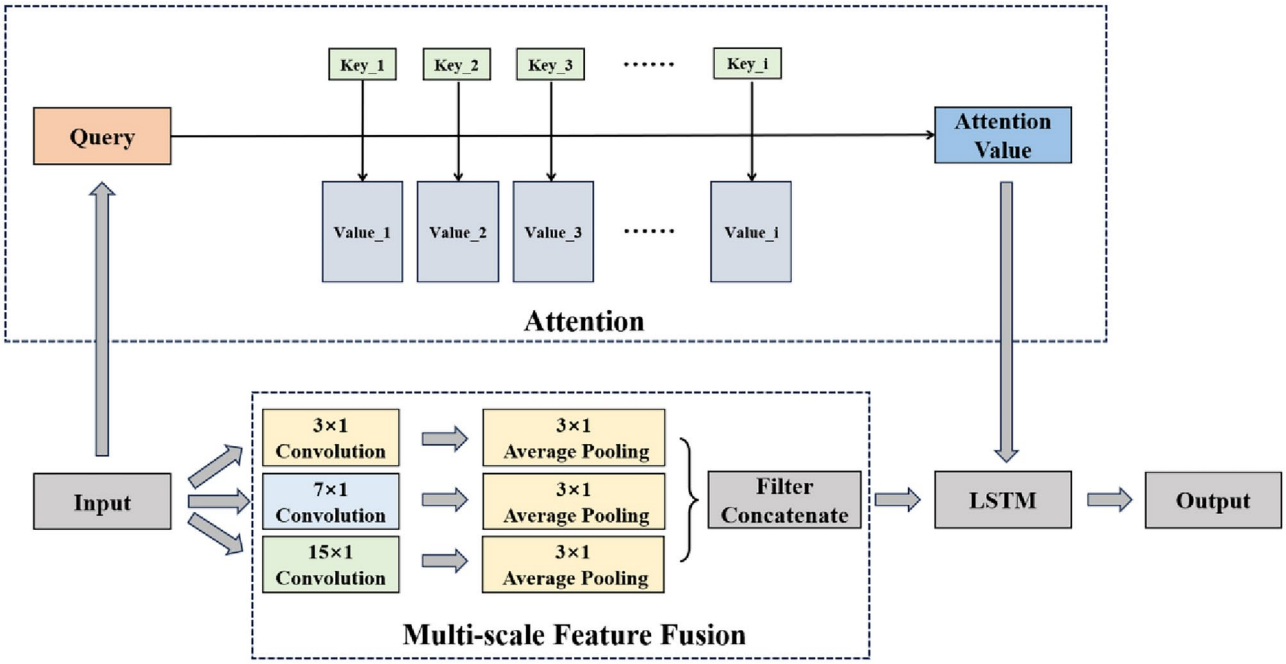

Fig. 3. An algorithmic framework based on neural networks for improved feature extraction by combining attention mechanisms and multi-scale feature fusion.

model to leverage the attention mechanism for richer feature representation. This significantly improves feature diversity and prediction accuracy, laying a solid foundation for model interpretability.

After investigating the extraction of artificial features by the attention mechanism, we found that these features are key to model identification and result analysis. Therefore, it is crucial to explore which features most significantly determine the ZT. These features were extracted from defect coding data. Defect encoding uses a 15-dimensional binary code that includes consecutive 1 s or 0 s quantity features (Consecutive_1s or Consecutive_0s) and pattern-specific quantity features (Patterns). Consecutive_1s_n represents the number of consecutive 1 s, Consecutive_0s_n represents the number of consecutive 0 s, Pattern_10 represents the number of '10' patterns, Pattern_0010 represents the number of '0010' patterns, and so on for other features. We examined different methods of feature importance scoring. Figure 5 depicts the distribution of SHapley Additive exPlanations (SHAP) values for various features on the model output. These values quantify each feature's contribution to the model prediction using a game-theoretic approach, allowing us to understand the importance of features and their impact on the model output.

Figure 5 ranks individual features based on the sum of their SHAP values across all samples, with SHAP value plots colored from blue to red indicating low to high feature values. This color coding helps visualize the positive and negative impacts of feature values on the model output. High values of the Consecutive_1s_2 feature (red) show significant positive contributions, while features like Pattern_101 also positively impact model predictions. Conversely, features such as Consecutive_0s_1 and Consecutive_1s_4 show weaker or even negative contributions at low values (blue). Figure 5a shows results from training with 500 data points, and Fig. 5b with 15,000 data points. Increased training data refines the model's understanding of feature impacts, but key features such as Consecutive_1s_1, Consecutive_1s_2, Consecutive_1s_3, Pattern_101, and Consecutive_0s_3 consistently demonstrate significant importance in both scenarios, underscoring their critical role in prediction.

Figure 6 illustrates the effectiveness of the CNN-LSTM model in predicting ZT values after incorporating high-contributing artificial features. The horizontal axis represents actual ZT values from NEGF calculations, while the vertical axis shows ZT values predicted by the model. Blue points indicate test set data, yellow points indicate training set data, and the red shaded area represents the error range between predicted and actual values. Most data points within the red shaded area and concentrated along the diagonal, indicating a high agreement between predicted and actual values. Specifically, the test set R^2 is 0.913, with an MSE of 0.00139 and an MAE of 0.057, demonstrating high prediction accuracy and stability. The training set data closely align with the diagonal, indicating good model fit during training. The test set data also show a desirable distribution, reflecting the model's strong generalization ability. Overall, Fig. 6 confirms that the inclusion of high-contributing artificial features significantly enhances the CNN-LSTM model's prediction performance, accurately predicting ZT values and highlighting the importance of these features in material property prediction.

In Fig. 7, we compare the density distributions of key features between the high ZT group ($ZT \geq 2.0$) and the low ZT group ($ZT \leq 1.5$), using both true and predicted ZT values. The vertical coordinate represents the probability density, indicating the frequency of occurrence of a given trait value. Density plots, which estimate the probability density function of a continuous variable, help us understand the pattern of feature distribution in different groups. The high ZT group (blue) and the low ZT group (red) show distinct feature value distributions,

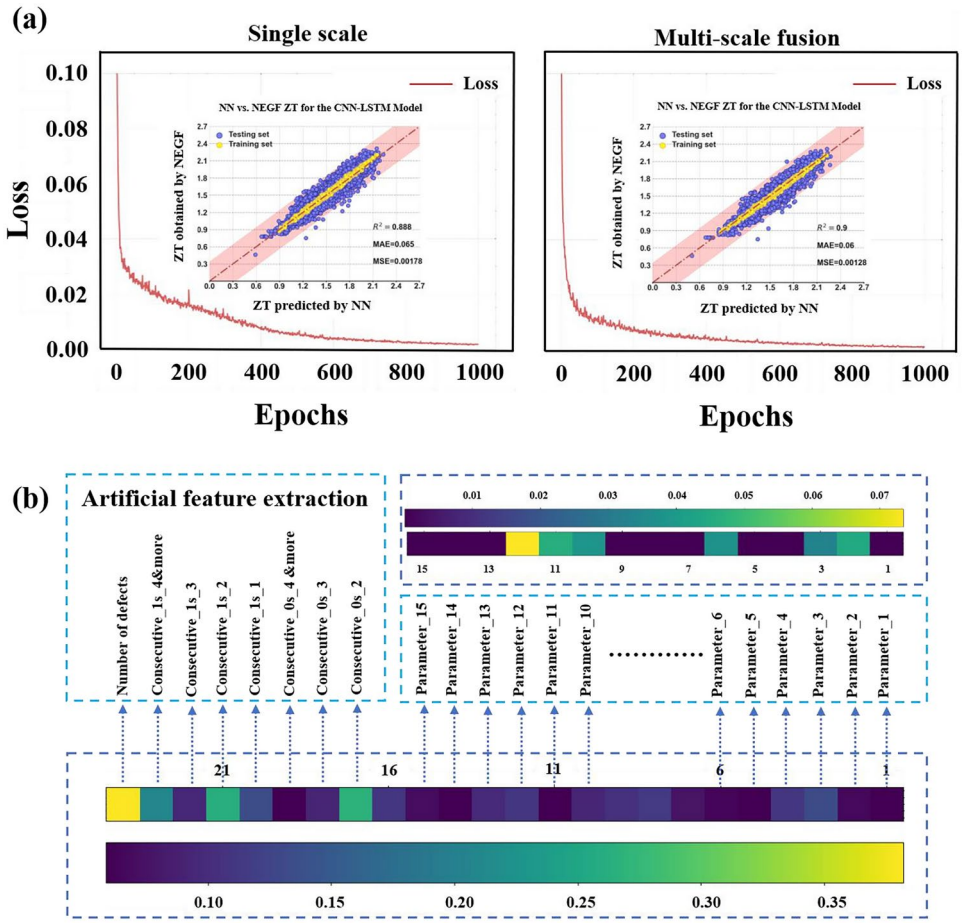

Fig. 4. Attention mechanisms and analysis results of multiscale feature fusion. Figure (**a**) shows a comparison of results using single-scale feature training and multiscale feature training, with the left inset showing the loss versus epochs curve and regression prediction results schematically for single-scale feature training and the right inset for multiscale training. Figure (**b**) shows the heat map of attention weights using the original binary coded features and the heat map of attention weights using the combination of binary coded and manually extracted features, where the manual feature extraction includes the number of defects with the underlying distribution.

providing insights into the features' impact on ZT values. The bottom part of Fig. 7 visually illustrates the structural patterns of defects corresponding to each feature. The center region of the γ-GYNR, delineated in red, highlights specific defect distributions and atomic configurations that define each feature type. For instance, defects represented by Consecutive_0s_1 (Fig. 7a) refer to single atomic vacancies positioned consecutively within the structure. In the high ZT group, this defect pattern is more evenly distributed with peaks between 2 and 5, whereas the low ZT group shows concentration between 1 and 3. Similarly, Consecutive_0s_2 (Fig. 7b) represents two consecutive vacancies, which lead to structural disruptions in the conjugated system, resulting in broader distributions in high ZT structures. The Pattern_101 feature (Fig. 7c) describes an alternating defect pattern within the atomic arrangement, contributing to stable transmission pathways in high ZT samples. Further defect types, such as Consecutive_1s_1, Consecutive_1s_2, Pattern_010, Pattern_01, Pattern_10, and Pattern_0110, show distinct defect distributions, particularly in high ZT configurations where these features are more diverse and dispersed. These visual representations of defect configurations provide a clearer understanding of how defect distribution impacts the ZT values. The high ZT group exhibits a more heterogeneous and dispersed pattern of defect features, while the low ZT group tends toward concentrated values.

The influence of short sequences of consecutive 1 s or 0 s plays a significant role in thermoelectric performance. From a physical standpoint, such defect patterns create localized disruptions in the atomic structure, which can lead to enhanced phonon scattering while preserving electron transport pathways. This selective scattering effect helps to reduce the thermal conductivity without compromising electronic conductivity, resulting in higher ZT values. Our NEGF calculations further support that an even distribution of these sequences contributes to stable transmission channels, minimizing disorder-induced scattering and facilitating efficient thermoelectric conversion. Consequently, configurations with evenly distributed short sequences of 1 s and 0 s achieve a favorable balance between electron transport and phonon scattering, enhancing thermoelectric performance. These distinct distribution patterns underscore the critical role of defect configurations in influencing

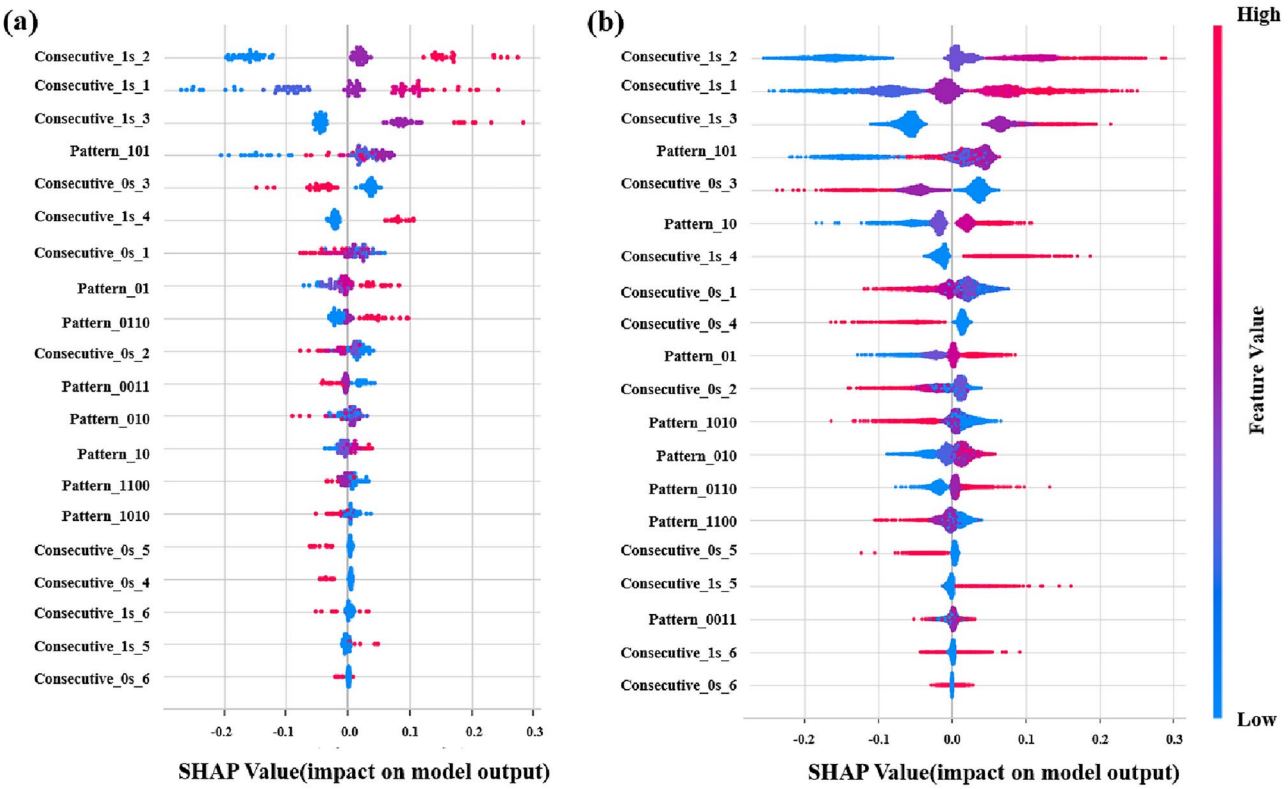

Fig. 5. An overview of the model importance, i.e. the shape value of each feature for each data point. The plot ranks each feature based on the sum of the SHAP values of all samples and uses the SHAP values to show the distribution of the influence of each feature on the model output. Colours indicate feature values (red, high; blue, low). Figures (**a**) and (**b**) show the results obtained using 500 and 15,000 data points for training, respectively.

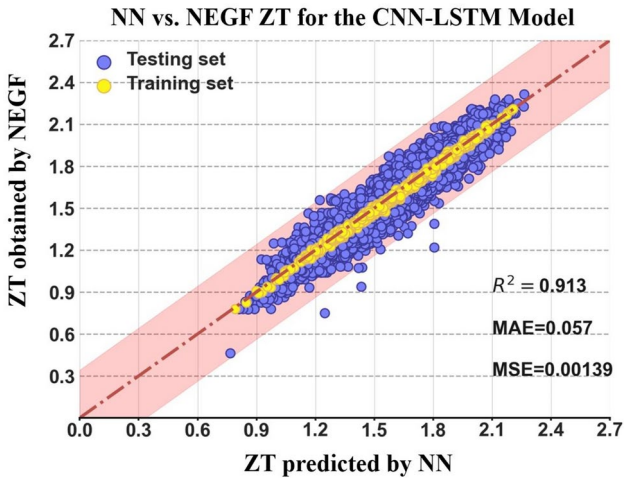

Fig. 6. Effect of model prediction after adding the screened high contribution artificial features. NN predicted vs. NEGF obtained ZT for the training set (yellow points on top of the blue points, representing 3% of the data) and the test set (blue points, representing 97% of the data).

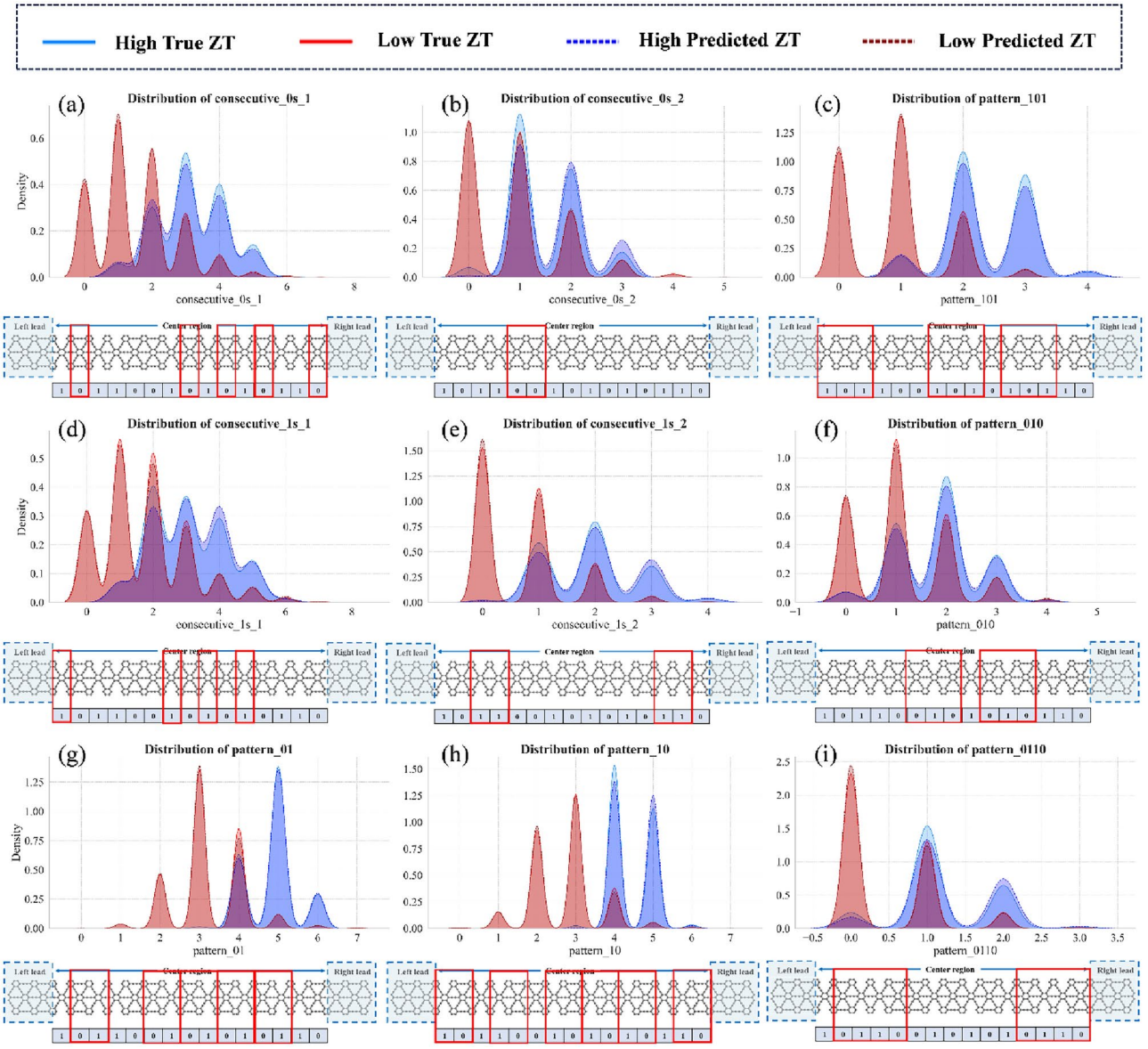

Fig. 7. Comparison of the density distributions of key features between the high ZT group (ZT ≥ 2.0) and low ZT group (ZT ≤ 1.5) for both true and predicted ZT values. The red areas represent the density distribution of the low true ZT group, while the blue areas represent the high true ZT group. The dashed lines indicate the predicted ZT values, with dark red and dark blue representing low and high predicted ZT groups, respectively.

thermoelectric performance. By integrating these features into the neural network, we successfully identified the top 30 defective γ-GYNR structures with the highest ZT values, as presented in Table 1. This detailed analysis provides valuable insights for optimizing model predictions and selecting impactful features for future studies.

Conclusions

In this study, the ZT values of edge disorder defective γ-GYNRs were comprehensively predicted and analyzed by combining binary coding, CNN-LSTM and multi-scale feature fusion methods. The ZT values of all 16,512 candidate structures were successfully predicted by the random sampling method with only 500 sets of initial structures, and the results showed that the average regression R^2 coefficient exceeded 0.91, and the average MAE was between 0.05 and 0.06. The analysis of the importance of the manually extracted features by SHAP values showed that single, dichotomous, and tricotomous defects had a significant effect on the prediction of ZT value. The samples in the high ZT group had significantly higher values for these features than the low ZT group, indicating the key role of specific defect orientation in enhancing thermoelectric properties. The density distribution of features in high and low ZT groups shows that high ZT group values are more diverse and dispersed, while low ZT group values are more concentrated. This corroborates the contribution of specific defect patterns to high ZT values. This study not only reveals the influence of the number and arrangement of defects in γ-GYNRs on the thermoelectric properties, but also demonstrates the effectiveness and accuracy of the

Parameter															ZT Predicted by NN	ZT Optained by NEGF	AE	ZT(NEGF)/ZT_{max}
1	**0**	**1**	**0**	**1**	**0**	**0**	**1**	**0**	**0**	**1**	**1**	**0**	**1**	**1**	**2.238307**	**2.3153975**	**0.167**	**1**
1	0	0	1	0	0	1	1	0	1	1	0	1	0	1	2.237062	2.2588491	0.112	0.975577
1	0	1	0	1	0	0	1	1	0	1	1	0	1	1	2.164955	2.2496424	0.085	0.971601
1	0	1	0	1	1	0	1	1	0	0	1	1	0	1	2.210099	2.2459142	0.036	0.969991
1	0	0	1	0	0	1	1	0	1	0	1	1	0	1	2.159045	2.2446485	0.086	0.969444
1	0	1	1	0	1	0	1	1	0	0	1	0	1	1	2.160061	2.2368953	0.077	0.966096
1	0	1	0	0	1	1	0	1	0	0	1	1	0	1	2.209407	2.2336686	0.024	0.964702
1	1	0	1	0	0	1	1	0	1	1	0	1	1	1	2.155402	2.2191119	0.064	0.958415
1	1	0	1	0	0	1	1	1	0	1	1	0	1	1	2.135201	2.2152729	0.080	0.956757
1	0	1	1	0	0	1	0	1	1	0	1	0	1	1	2.137593	2.2137568	0.076	0.956102
1	0	1	1	0	1	0	1	0	0	1	1	0	1	1	2.135032	2.2132957	0.078	0.955903
1	0	0	1	0	1	0	1	1	0	0	1	0	1	1	2.208146	2.2119627	0.004	0.955327
1	0	1	0	0	1	0	0	1	1	0	1	1	0	1	2.222272	2.2062948	0.016	0.952879
1	0	1	0	1	0	0	1	1	0	0	1	1	0	1	2.189777	2.2016733	0.012	0.950884
1	0	1	1	0	0	1	1	0	1	1	0	1	1	1	2.140429	2.1854968	0.045	0.943897
1	0	1	0	1	1	0	0	1	0	0	1	1	0	1	2.188665	2.183625	0.005	0.943089
1	0	1	0	1	0	1	1	0	0	1	1	0	1	1	2.151502	2.1812751	0.030	0.942074
1	0	1	1	0	0	1	0	0	1	0	1	1	0	1	2.136352	2.1803205	0.044	0.941661
1	0	1	0	0	1	0	1	1	0	1	1	0	1	1	2.165362	2.1781042	0.013	0.940704
1	0	1	0	0	1	0	1	1	0	0	1	1	0	1	2.247539	2.1772337	0.070	0.940328
1	0	1	0	0	1	0	1	1	1	0	1	1	0	1	2.215779	2.1769958	0.039	0.940226
0	1	0	1	0	1	0	0	1	1	0	1	1	0	1	2.15565	2.1721017	0.016	0.938112
1	0	0	1	0	0	1	1	0	1	1	0	1	1	1	2.14428	2.1674476	0.023	0.936102
0	1	0	0	1	1	0	1	1	0	0	1	0	1	1	2.160074	2.1656911	0.006	0.935343
1	0	1	0	0	1	1	0	1	1	0	1	1	0	1	2.225394	2.1619358	0.063	0.933721
0	1	0	0	1	1	0	1	1	0	0	1	1	0	1	2.155305	2.1587946	0.003	0.932365
0	1	1	0	1	1	0	0	1	0	0	1	1	0	1	2.16885	2.1567254	0.012	0.931471
1	0	1	1	0	0	1	0	1	1	0	1	1	0	1	2.221826	2.1445601	0.077	0.926217
1	0	1	1	0	0	1	1	0	1	0	1	1	0	1	2.17712	2.1361713	0.041	0.922594
1	0	1	1	0	1	1	0	1	0	0	1	0	1	1	2.154536	2.116173	0.038	0.913957

Table 1. Neural network prediction of the set of descriptors for the 30 defective γ-GYNRs with the highest ZT values and their predicted and theoretically calculated values.

proposed method. Through feature extraction and screening, the constructed neural network model performs well in predicting the thermoelectric properties of low-dimensional edge-disordered defective materials. These results provide new methods and perspectives for the design and exploration of other low-dimensional materials with excellent thermoelectric properties, and demonstrate the great potential of our constructed neural network algorithms in materials science research.

Data availability

The data that support the findings of this study are available from the corresponding author upon reasonable request. Additional data, including datasets generated during the current study, are available on GitHub at https://github.com/guojiayi0331/CNN-LSTM_ZT_Gamma-Graphyne.

Code availability

The code used in this study for the CNN-LSTM model and ZT prediction of γ-GYNRs structures is openly available on GitHub at https://github.com/guojiayi0331/CNN-LSTM_ZT_Gamma-Graphyne.

Received: 10 August 2024; Accepted: 19 December 2024
Published online: 07 January 2025

References

1. Di Salvo,. Thermoelectric cooling and power generation. *Science* **285**, 703–706. https://doi.org/10.1126/science.285.5428.703 (1999).
2. Jia, N. et al. Thermoelectric materials and transport physics. *Mater. Today. Phys.* **21**, 100519. https://doi.org/10.1016/j.mtphys.2021.100519 (2021).
3. Mao, J., Chen, G. & Ren, Z. F. Thermoelectric cooling materials. *Nat. Mater.* **20**, 454–461. https://doi.org/10.1038/s41563-020-00852-w (2021).
4. Zhou, Y. M. & Zhao, L. D. Promising thermoelectric bulk materials with 2D structures. *Adv. Mater.* **29**, 1702676. https://doi.org/10.1002/adma.201702676 (2017).

5. Heremans, J. P. et al. Enhancement of thermoelectric efficiency in PbTe by distortion of the electronic density of states. *Science* **321**, 554–557. https://doi.org/10.1126/science.1159725 (2008).
6. Hong, M., Li, M., Wang, Y., Shi, X. L. & Chen, Z. G. Advances in versatile GeTe thermoelectrics from materials to devices. *Adv. Mater.* **35**, 2208272. https://doi.org/10.1002/adma.202208272 (2023).
7. Poudel, B. et al. High-thermoelectric performance of nanostructured bismuth antimony telluride bulk alloys. *Science* **320**, 634–638. https://doi.org/10.1126/science.1156446 (2008).
8. Yao, H. Y. et al. Recent development of thermoelectric polymers and composites. *Macromol. Rapid. Comm.* **39**, 1700727. https://doi.org/10.1002/marc.201700727 (2018).
9. Dresselhaus, M. S. et al. New directions for low-dimensional thermoelectric materials. *Adv. Mater.* **19**, 1043–1053 (2007).
10. Chen, G., Dresselhaus, M., Dresselhaus, G., Fleurial, J.-P. & Caillat, T. Recent developments in thermoelectric materials. *Int. Mater. Rev.* **48**, 45–66 (2003).
11. Hébert, S. et al. Searching for new thermoelectric materials: Some examples among oxides, sulfides and selenides. *J. Phys-Condens. Mat.* **28**, 013001. https://doi.org/10.1088/0953-8984/28/1/013001 (2016).
12. Dresselhaus, M. et al. The promise of low-dimensional thermoelectric materials. *Nanosc. Microsc. Therm.* **3**, 89–100 (1999).
13. Novoselov, K. S. et al. Electric field effect in atomically thin carbon films. *Science* **306**, 666–669. https://doi.org/10.1126/science.1102896 (2004).
14. Bhimanapati, G. R. et al. Recent advances in two-dimensional materials beyond graphene. *Acs. Nano* **9**, 11509–11539. https://doi.org/10.1021/acsnano.5b05556 (2015).
15. Tan, C. L. et al. Recent advances in ultrathin two-dimensional nanomaterials. *Chem. Rev.* **117**, 6225–6331. https://doi.org/10.1021/acs.chemrev.6b00558 (2017).
16. Fang, Y., Liu, Y. X., Qi, L., Xue, Y. R. & Li, Y. L. 2D graphdiyne: an emerging carbon material. *Chem. Soc. Rev.* **51**, 2681–2709. https://doi.org/10.1039/d1cs00592h (2022).
17. Peng, Q. et al. New materials graphyne, graphdiyne, graphone, and graphane: Review of properties, synthesis, and application in nanotechnology. *Nanotechnol. Sci. Appl.* **7**, 1–29. https://doi.org/10.2147/nsa.S40324 (2014).
18. Kang, J., Wei, Z. & Li, J. Graphyne and its family: Recent theoretical advances. *ACS Appl. Mater. Interfaces* **11**, 2692–2706 (2018).
19. Malko, D., Neiss, C., Viñes, F. & Görling, A. Competition for graphene: Graphynes with direction-dependent dirac cones. *Phys. Rev. Lett.* **108**, 086804. https://doi.org/10.1103/PhysRevLett.108.086804 (2012).
20. Qi, S. Y. et al. Two-dimensional graphyne-like carbon nitrides: Moderate band gaps, high carrier mobility, high flexibility and type-II band alignment. *Carbon* **149**, 234–241. https://doi.org/10.1016/j.carbon.2019.04.024 (2019).
21. Chen, J. M., Xi, J. Y., Wang, D. & Shuai, Z. G. Carrier mobility in graphyne should be even larger than that in graphene: A theoretical prediction. *J. Phys. Chem. Lett.* **4**, 1443–1448. https://doi.org/10.1021/jz4005587 (2013).
22. Qian, X. M. et al. Construction of graphdiyne nanowires with high-conductivity and mobility. *Dalton. T.* **41**, 730–733. https://doi.org/10.1039/c1dt11641j (2012).
23. Tang, Y. Q., Yang, H. Y. & Yang, P. Investigation on the contact between graphdiyne and Cu (111) surface. *Carbon* **117**, 246–251. https://doi.org/10.1016/j.carbon.2017.02.097 (2017).
24. Cranford, S. W. & Buehler, M. J. Mechanical properties of graphyne. *Carbon* **49**, 4111–4121. https://doi.org/10.1016/j.carbon.2011.05.024 (2011).
25. Narita, N., Nagai, S., Suzuki, S. & Nakao, K. Optimized geometries and electronic structures of graphyne and its family. *Phys. Rev. B.* **58**, 11009 (1998).
26. He, F. & Li, Y. Advances on theory and experiments of the energy applications in graphdiyne. *CCS. Chem.* **5**, 72–94 (2023).
27. Li, Y. J., Xu, L., Liu, H. B. & Li, Y. L. Graphdiyne and graphyne: From theoretical predictions to practical construction. *Chem. Soc. Rev.* **43**, 2572–2586. https://doi.org/10.1039/c3cs60388a (2014).
28. Niu, G. S. et al. Graphdiyne and its derivatives as efficient charge reservoirs and transporters in semiconductor devices. *Adv. Mater.* **35**, 2212159. https://doi.org/10.1002/adma.202212159 (2023).
29. Zhao, F. G. et al. Precise preparation of triarylboron-based graphdiyne analogues for gas separation. *Angew. Chem. Int. Edit.* **63**, e202317294. https://doi.org/10.1002/anie.202317294 (2024).
30. Jia, Z. Y. et al. Synthesis and properties of 2D carbon-graphdiyne. *Acc. Chem. Res.* **50**, 2470–2478. https://doi.org/10.1021/acs.accounts.7b00205 (2017).
31. Liu, Q., Wang, X., Jing, Y. & Wang, J. Graphyne and graphdiyne nanoribbons: from their structures and properties to potential applications. *Phys. Chem. Chem. Phys.* **26**(3), 1541–1563. https://doi.org/10.1039/D3CP04393B (2024).
32. Ali, S. & Sun, M. Electronic, thermoelectric and electrical transport properties of single layer γ-graphyne. *Mater. Sci. Eng. B* **306**, 117454 (2024).
33. Li, G. X. et al. Architecture of graphdiyne nanoscale films. *Chem. Commun.* **46**, 3256–3258. https://doi.org/10.1039/b922733d (2010).
34. Zhou, W. X. et al. Controllable synthesis of graphdiyne nanoribbons. *Angew. Chem. Int. Edit.* **59**, 4908–4913. https://doi.org/10.1002/anie.201916518 (2020).
35. Yeo, J. et al. Multiscale design of graphyne-based materials for high-performance separation membranes. *Adv. Mater.* **31**, 1805665 (2019).
36. Bolding, C. M. et al. Edge functionalization of bulk γ-graphyne facilitates mechanical exfoliation and modulates the mode of sheet stacking. *J. Am. Chem. Soc.* **146**, 12889–12894 (2024).
37. Wang, X. M., Mo, D. C. & Lu, S. S. On the thermoelectric transport properties of graphyne by the first-principles method. *J. Chem. Phys.* **138**, 204704. https://doi.org/10.1063/1.4806069 (2013).
38. Sevinçli, H. & Sevik, C. Electronic, phononic, and thermoelectric properties of graphyne sheets. *Appl. Phys. Lett.* **105**, 223108. https://doi.org/10.1063/1.4902920 (2014).
39. Chen, Y., Jayasekera, T., Calzolari, A., Kim, K. W. & Nardelli, M. B. Thermoelectric properties of graphene nanoribbons, junctions and superlattices. *J. Phys-Condens. Mat.* **22**, 372202. https://doi.org/10.1088/0953-8984/22/37/372202 (2010).
40. Kim, W. et al. Thermal conductivity reduction and thermoelectric figure of merit increase by embedding nanoparticles in crystalline semiconductors. *Phys. Rev. Lett.* **96**, 045901. https://doi.org/10.1103/PhysRevLett.96.045901 (2006).
41. Li, N. et al. Optimizing the thermoelectric performance of graphyne nanotube via applying radial strain. *J. Appl. Phys.* **121**, 125112. https://doi.org/10.1063/1.4979308 (2017).
42. Ouyang, T. & Hu, M. Thermal transport and thermoelectric properties of beta-graphyne nanostructures. *Nanotechnology* **25**, 245401. https://doi.org/10.1088/0957-4484/25/24/245401 (2014).
43. Xie, G. F., Ding, D. & Zhang, G. Phonon coherence and its effect on thermal conductivity of nanostructures. *Adv. Phys-X* **3**, 719–754. https://doi.org/10.1080/23746149.2018.1480417 (2018).
44. Yaremchenko, A. A. et al. Boosting thermoelectric performance by controlled defect chemistry engineering in Ta-substituted strontium titanate. *Chem. Mater.* **27**, 4995–5006. https://doi.org/10.1021/acs.chemmater.5b01389 (2015).
45. Xie, G. F. et al. Ultra-low thermal conductivity of two-dimensional phononic crystals in the incoherent regime. *Npj. Comput. Mater.* https://doi.org/10.1038/s41524-018-0076-9 (2018).
46. Yamawaki, M., Ohnishi, M., Ju, S. H. & Shiomi, J. Multifunctional structural design of graphene thermoelectrics by Bayesian optimization. *Sci. Adv.* https://doi.org/10.1126/sciadv.aar4192 (2018).
47. Choudhary, K., Garrity, K. F. & Tavazza, F. Data-driven discovery of 3D and 2D thermoelectric materials. *J. Phys-Condens. Mat.* https://doi.org/10.1088/1361-648X/aba06b (2020).

48. Han, G. S., Sun, Y. X., Feng, Y. N., Lin, G. & Lu, N. Artificial intelligence guided thermoelectric materials design and discovery. *Adv. Electron. Mater.* **9**, 2300042. https://doi.org/10.1002/aelm.202300042 (2023).
49. Sheng, Y. et al. Active learning for the power factor prediction in diamond-like thermoelectric materials. *Npj. Comput. Mater.* https://doi.org/10.1038/s41524-020-00439-8 (2020).
50. Zhu, T. S. et al. Charting lattice thermal conductivity for inorganic crystals and discovering rare earth chalcogenides for thermoelectrics. *Energ. Environ. Sci.* **14**, 3559–3566. https://doi.org/10.1039/d1ee00442e (2021).
51. Al-Fahdi, M., Yuan, K. P., Yao, Y. G., Rurali, R. & Hu, M. High-throughput thermoelectric materials screening by deep convolutional neural network with fused orbital field matrix and composition descriptors. *Appl. Phys. Rev.* **11**, 021402. https://doi.org/10.1063/5.0187855 (2024).
52. Cui, C. F. et al. Bayesian optimization-based design of defect gamma-graphyne nanoribbons with high thermoelectric conversion efficiency. *Carbon* **176**, 52–60. https://doi.org/10.1016/j.carbon.2021.01.126 (2021).
53. Yamamoto, T. & Watanabe, K. Nonequilibrium Green's function approach to phonon transport in defective carbon nanotubes. *Phys. Rev. Lett.* **96**, 255503. https://doi.org/10.1103/PhysRevLett.96.255503 (2006).
54. Datta, S. *Electronic transport in mesoscopic systems* (Cambridge University Press, 1997).

Acknowledgements

This work is supported by the National Natural Science Foundation of China (No. 12204398 and 52303340). National Key Research and Development Program of China (2022YFC2205003). Technology Innovation Program of Hunan Province (2022RC3027) and the Department of Science and Technology of Hunan Province (2023JJ40617).

Author contributions

J.G. conducted formal analysis, investigation, and visualization, and was responsible for software development and writing the original draft. C.C. contributed to conceptualization and data curation, sharing equal responsibility for methodology development. T.O. provided supervision and contributed equally to writing the review and editing. J.C. acquired funding and provided equal supervision. X.W. was responsible for conceptualization, funding acquisition, and contributed equally to writing the review and editing.

Declarations

Competing interests

The authors declare no competing interests.

Additional information

Supplementary Information The online version contains supplementary material available at https://doi.org/10.1038/s41598-024-84074-z.

Correspondence and requests for materials should be addressed to J.C. or X.W.